Chemical Engineering Journal 492 (2024) 152192

Contents lists available at ScienceDirect

Chemical Engineering Journal

journal homepage: www.elsevier.com/locate/cej

Microwave antenna focusing for spatially resolved modulation of burn rate

Keren Shi, Yujie Wang, Michael R. Zachariah *

University of California, Riverside, CA 92521, United States

A R T I C L E I N F O

Keywords:
Microwave stimulation
Combustion modulation
Nanothermites

A B S T R A C T

This study explores the ability to dynamically modulate the burn rate of nanothermites through microwave generated heat zones. These heat zones were generated by embedding a microwave receiving antenna in 3D printed Al/CuO samples. These thermal hot spots in the nanothermites are generated by the induced high electric fields at the terminus of an embedded receiving antenna and are monitored by an IR camera. The burn rates were investigated for different MW induced hot spot temperatures, geometries and receiving antenna materials. The local burn rate increase closely tracks the hot spot spatial distribution, and for our experimental condition enabled an amplification of burn rate of ~6×. An effective burn rate activation energy was calculated to be ~18 kJ/mol from the Arrhenius plot of local burn rate and initial temperature. Three color pyrometry confirms that the main mechanism of the local burn rate increase is related to the initial temperature profile in the sample. This study demonstrates the sensitivity of the local burn rate of nanothermites to initial temperature and provides a new approach to modulate the burn rate by localizing MW energy.

1. Introduction

Compared to a conventional liquid propellant, solid propellants offer simplified motor design and safe storage [1,2]. However, after ignition, the regression rate operates at steady-state though a symbiotic relationship between chemistry and transport. As such a solid propellant cannot be throttled [3,4]. These disadvantages greatly limit the application mainly to rocket boosters [5]. Electric control and laser assistance have been explored to control the ignition of solid propellants. Gobin et al. developed an electrically controlled solid propellant whereby the ignitability can be controlled with an applied voltage across the propellant by addition of polyethylene oxide [6]. Duan et al. studied laser-controlled solid propellant by doping carbon black into ammonium perchlorate (AP)-based propellant, repeatable ignitions could be achieved to moderate the overall burn rate [7]. Considerable effect has also been expended to manipulate the burn rate of solid propellants through motor design or additives [8–13], although in the latter case unless the additives are dispersed in a pre determined distribution modulation of the burn rate cannot be achieved. In any case dynamic modulation is still not possible. The pintle nozzle technology can control the burn rate by varying the chamber pressure [8]. Electromagnetic stimulation offers the potential to selectively focus energy, dynamically modulate the delivery of energy, and with appropriate choice of wavelength and absorber deposition energy at least in principle deep within a grain. Isakari et al. demonstrated that the burn rate of AP/HTPB propellant can be controlled by laser heating at the burning surface [14]. Barkley et al. explored the microwave region and showed that microwave (MW) energy can be deposited into the gaseous and condensed phase product of Al/AP propellant and further improve the burn rate [15]. Since most components of energetic materials are either transparent or weakly absorbing in the MW frequency region, an opportunity presents itself to manipulate the burn rate by adding spatially distributed MW sensitizers through additive manufacturing approaches [16].

In this work, spatial modulated burn rate is demonstrated for 3D printed nanothermites by embedded a receiving antenna to localize MW energy. Metal wires were embedded into high loading Al/CuO nanothermites during direct write fabrication. The metal wires act as a *receiving antenna* within the sample, *inducing high electric fields at the wire terminus*, and thus dielectric heat the nanothermites (not the wire). We observe, through high-speed camera videography and pyrometry an increase in the local burn rates corresponding to the location of the microwave induced hotspots. These burn rates augmentations were investigated with respect to hot spot temperature, geometries and receiving antenna material. Results show that the peak burn rates increase by up to 6×, and can be controlled by location of the embedded receiving antenna. Three color pyrometry shows that the mechanism of the burn rates increase depends on hot spot temperature profile. An effective thermal activation energy is calculated to be ~18 kJ/mol,

---

* Corresponding author.
E-mail address: mrz@engr.ucr.edu (M.R. Zachariah).

https://doi.org/10.1016/j.cej.2024.152192
Received 16 December 2023; Received in revised form 9 May 2024; Accepted 11 May 2024

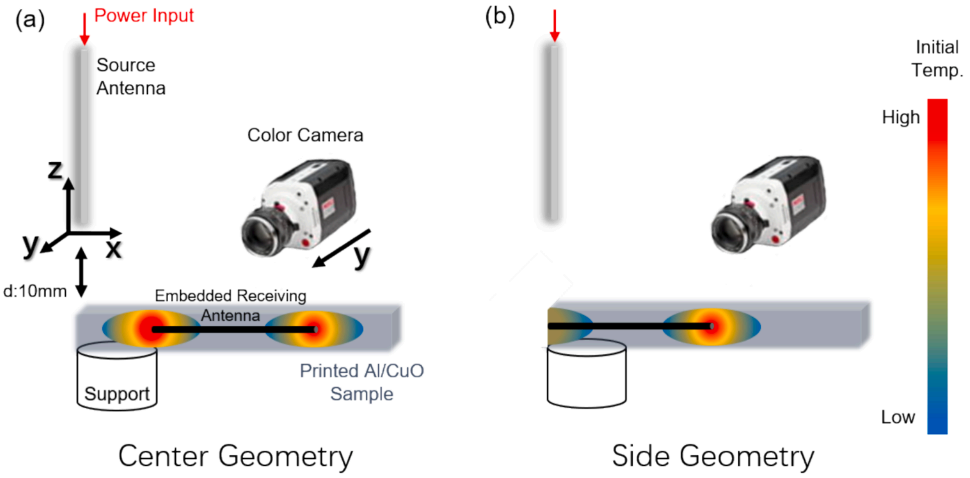

Fig. 1. Experiment setup of (a) center geometry: with receiving antenna embedded in the center of Al/CuO nanothermites. (b) Side geometry: with receiving antenna embedded in the left side of the sample. Color gradient represents the two hot spots generated at the terminals of the receiving antenna. Only the right hot spots were analyzed in this paper.

which suggests some type of transport control due to its relatively low value. This study demonstrates a new approach to estimate the sensitivity of burn rate of a solid propellant to initial temperature and a methodology to dynamically modulate the burn rate of solid propellant through localized MW energy.

2. Experimental section

2.1. Materials

Aluminum (Al) nanoparticles (80 nm, 67 wt% active content determined by thermogravimetric analysis) and copper oxide (CuO) nanoparticles (40 nm) were obtained from Novacentrix Inc. and U.S. Research Nanomaterials, respectively. METHOCEL™ F4M hydroxypropyl methylcellulose (HPMC) and Poly(vinylidene fluoride) (PVDF) were obtained from Dow Chemical Co. and Sigma-Aldrich. N,N-Dimethylformamide (DMF, 99.8 %) was obtained from Fisher Scientific. Nichrome (NiCr) wire (diameter of 0.25 mm) was purchased from Ted Pella, Inc. Aluminum (Al) wire (diameter of 0.25 mm) was purchased from Fisher Scientific. All materials were used as received.

2.2. Direct writing ink preparation and sample fabrication

The high loading Al/CuO nanothermites samples with embedded receiving antennas were fabricated through a direct writing process [17]. First, the high loading ink was prepared by dissolving 4 wt% PVDF, 6 wt% HPMC and 90 wt% total of Al and CuO nanoparticles (equivalence ratio, $\varphi = 1$) in DMF with a loading of 312.5 mg/ml. A total of 15 layers of nanothermites were printed. The receiving antennas, NiCr and Al wires, were cut into 20 mm ($\sim 1/6\lambda$) and embedded onto the 10th printed layer to generate localized hot spots. The printed samples were cut into 40 mm ($\sim 1/3\lambda$) sticks. Two embedded antennas geometries and two different receiving antenna materials (NiCr and Al) were tested as shown in Fig. 1.

2.3. Experiment setup

The microwave (MW) source antenna was made from 30 mm ($\sim 1/4\lambda$) 2 % thoriated tungsten electrode (diameter: 1 mm) and powered by the magnetron (MKS Instruments, MW head TM012) operating at 2.45 GHz ($\lambda \sim 122$ mm) [18]. The propellants with receiving antennas were supported 10 mm below the source antenna by alumina crucibles. The experimental configuration is shown in Fig. 1 and Fig. S1.

2.4. High-speed color imaging and infrared imaging

An infrared (IR) camera (Telops, FAST M3K) was used to image the localized hot spot temperatures before ignition (exposure time: 10 μs, frame rate: 100 fps, resolution: ~140 μm per pixel). The MW was first powered on, and the IR camera was used to monitor the hot spot temperature on the sample surface. Once the hot spots reached a desired temperature, the MW was maintained at the same power for another ~10 s to allow the sample temperature to maintain a steady state (source antenna power required to generate different hot spots temperature are listed in Table S1). The samples were ignited by a secondary heat source at the right side of sample. A high-speed color camera (Vision Research Phantom, Miro M110) was used to record the combustion process (exposure time: 24 μs, frame rate: 5000 fps, resolution: ~60 μm per pixel). The MW source was kept at the same power during the combustion process to maintain the hot spots temperature.

2.5. Local burn rate and flame temperature measurement

The burn rate (v) was extracted from the color imaging using a custom MATLAB routine. First, the color images were binarized into black (unreacted zone) and white (flame zone) images and the position (x) of the burning surface was determined from the center line on the sample for each frame, an example was demonstrated in Fig. S2 [19]. Then the local burn rate was calculated as dx/dt. The flame temperature was determined by color pyrometry [20,21]. Three channel intensities (red, green and blue) were extracted from the color imaging and their ratios was used to calculate the flame temperature. The color camera system was calibrated with a blackbody source (Mikron M390) and the calculated temperature uncertainty was estimated to be ~200–300 K. All experiments were repeated in triplicate unless otherwise stated.

2.6. Hot spot heating rate measurement and electric field simulation

MW heating rates were determined from a linear fit of the temporal temperature of the right hot spots under different MW source antenna. The induced electric field was simulated by COMSOL using the experimental configuration of the source and receiving antenna as shown in Fig. 1 (simulation model is illustrated in Fig. S3). The physical properties of tungsten (source antenna) and aluminum (receiving antenna) were taken from the COMSOL build-in database. The electric conductivity of NiCr (receiving antenna) is 1×10^6 S/m [22]. The Al/CuO nano particles and polymer matrix are not included in the model. Since both Al and CuO nano particles are non-magnetic and the heating mechanism is

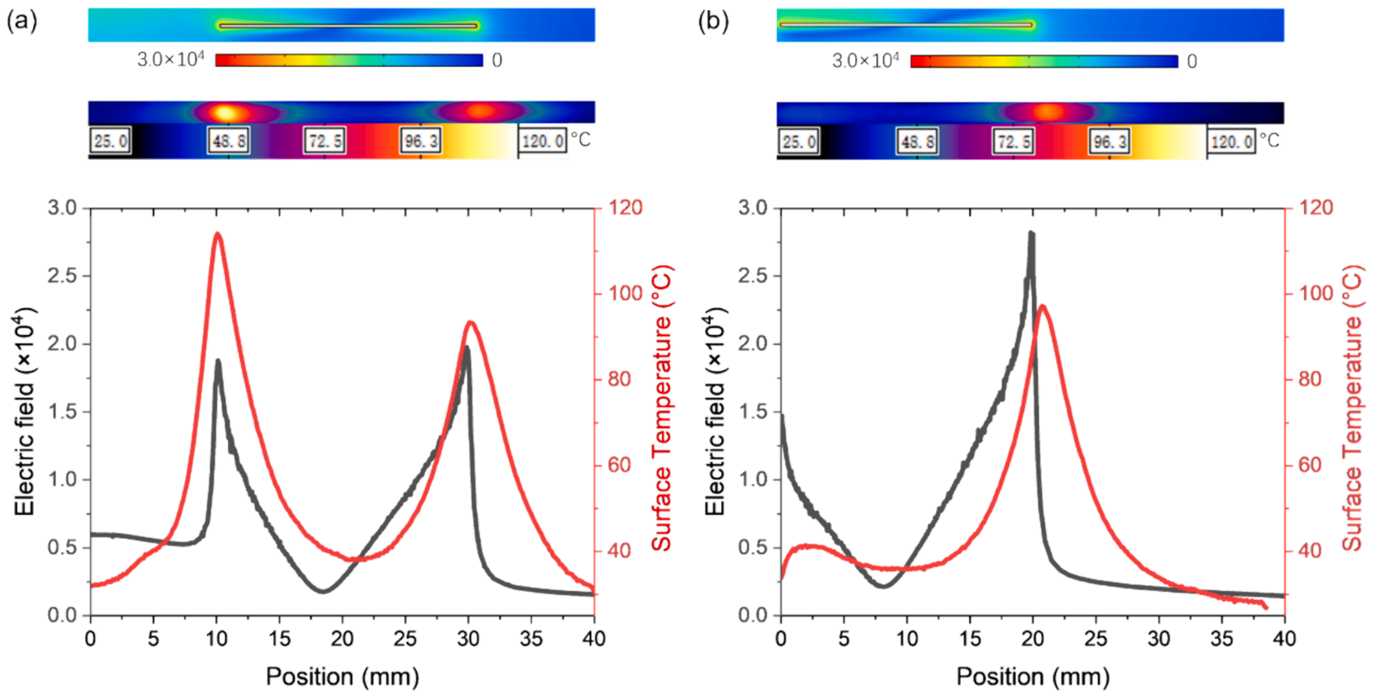

Fig. 2. Spatial distribution of the calculated induced electric field and the measured temperature distribution of (a) center geometry and (b) side geometry. (Top: simulated electric field distribution from COMSOL. Middle: IR image of the initial hot spot at ~100 °C before ignition. Bottom: electric field and surface temperature distribution along the central line.

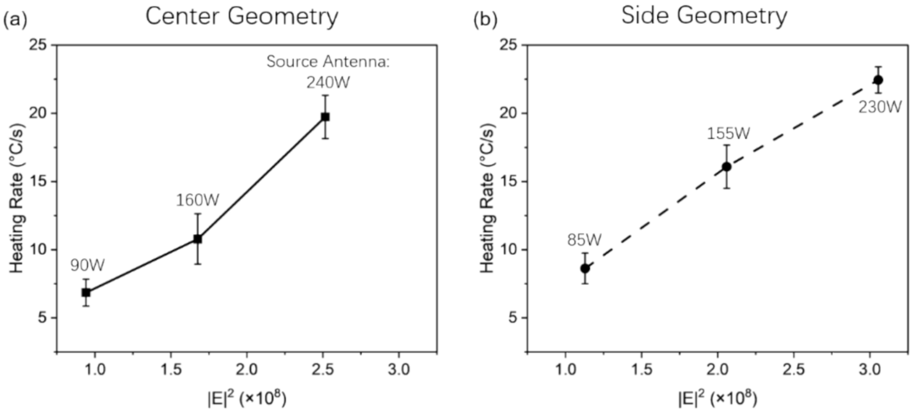

Fig. 3. Measured heating rate at (right) hot spot of (a) center geometry and (b) side geometry increases with the square of the electric field calculated from COMSOL simulation at different source antenna power.

dielectric heating [23], only the induced electric field was simulated and further compared to the measured heating rate.

3. Results and discussion

3.1. Local burn rate at the hot spots

In our previous studies, we have shown that two localized thermal hot spots are generated at the two terminal positions of the embedded receiving antennas in Al/CuO samples via remote MW stimulation, due to the enhanced electric field there [18]. Unlike the previous experiment setup, the samples were suspended by alumina supports placed under the source antenna to conduct burn rate measurements. In the center geometry, the left hot spots have a higher steady state temperature than the right which is attributed to edge effects from the support. In the side geometry, the supports act as a heat sink so the heating effect of the left hot spot was not significant. Furthermore, smoke generated during combustion can obscure imaging and in some cases, arcing occurs when the flame approaches the source antenna [24]. As such for the purposes of results presentation and analysis only the right hot spots of the two geometries were used.

Fig. 2 shows the spatial correspondence of electric field distribution in the sample and the measured temperature. Quite clearly there is a direct correlation of the antenna induced electric field and the corresponding temperature in the sample. The results presented in Fig. 2 are the steady-state temperature. On theoretical grounds, however we expect the heating rate ($\Delta T/t$) to scale as the square of the electric field strength ($|E|$) [25].

$$\frac{\Delta T}{t} = \frac{\omega \varepsilon_0 \varepsilon' \tan\delta}{\rho C}|E|^2 \quad (1)$$

Where ω is the angular frequency, ε_0 is the vacuum permittivity, ε' and $\tan\delta$ are the real part of the relative permittivity and the loss tangent, ρ is

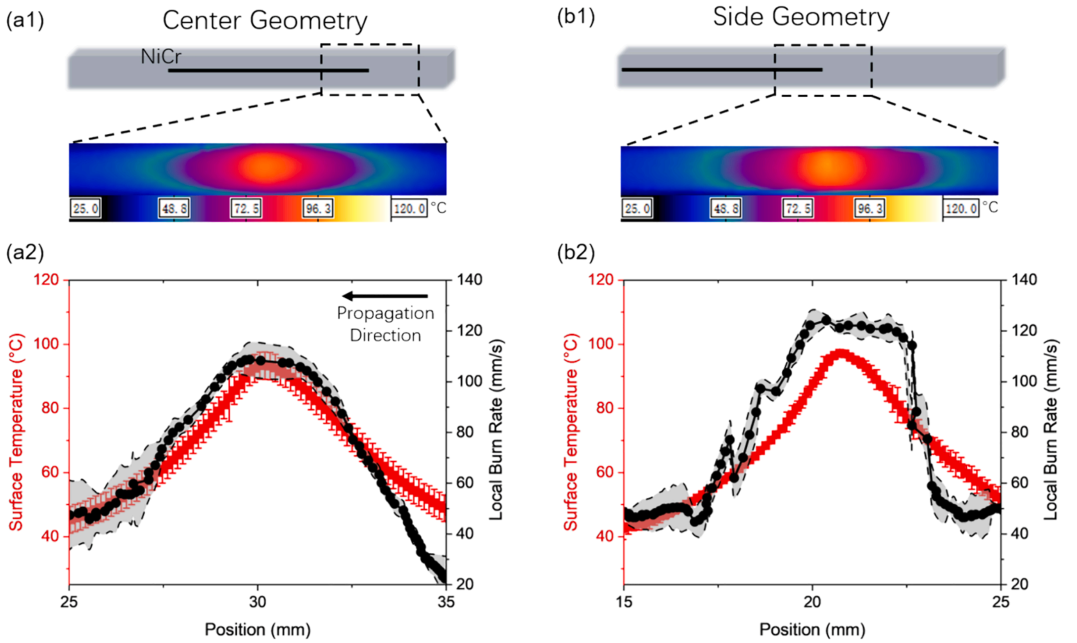

Fig. 4. Diagram of the (a1) center geometry and (b1) side geometry of the embedded NiCr receiving antenna in Al/CuO samples and the IR image of the initial hot spot at ~100 °C before ignition (Video S2). (a2) and (b2) Local burn rates change with surface hot spot temperature at ~100 °C (Video S3). (Note: only the burn rates at the right hot spots were analyzed).

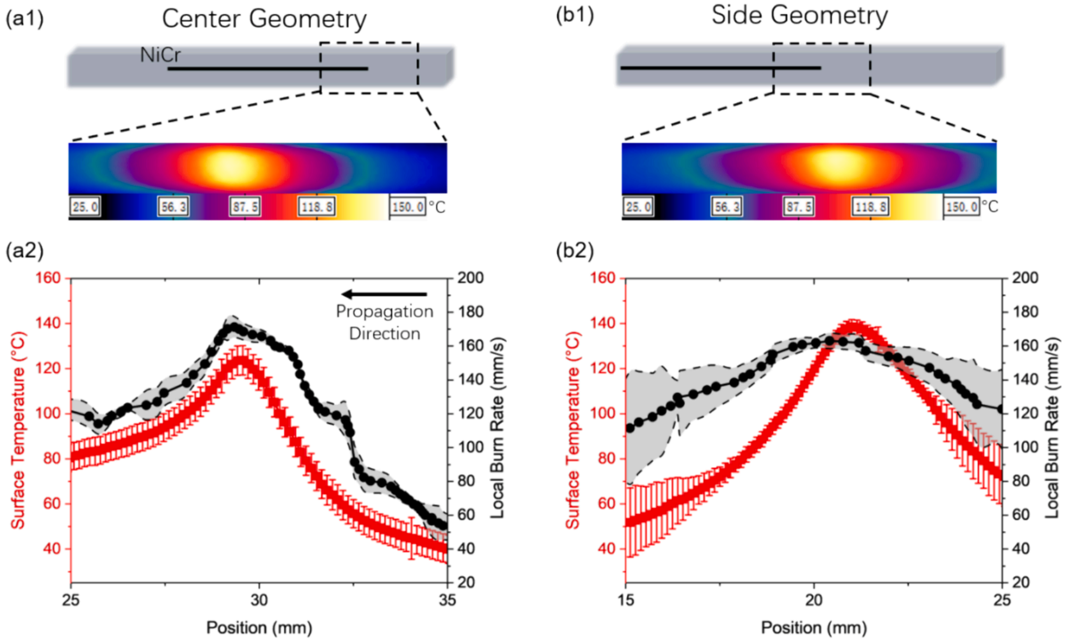

Fig. 5. Diagram of the (a1) center geometry and (b1) side geometry of the embedded NiCr receiving antenna in Al/CuO samples and the IR image of the initial hot spot at ~150 °C before ignition. (a2) and (b2) Local burn rates change with surface hot spot temperature at ~150 °C. (Note: only the burn rates at the right hot spots were analyzed).

density, *C* is the specific heat capacity. The results we observe are consistent with Eq. (1) and are presented in Fig. 3.

This behavior has been discussed in more detail from our prior work, and the reader is reminded that the receiving antenna is not being heated by the MW's (Fig. S4) rather the large electric field generated induces dielectric heating in the surrounding sample [18].

To study the effect of MW heating on burn rate we chose to conduct experiments where the material temperature achieved a steady-state prior to beginning the experimental burn measurements. Before ignition, MW exposure at different power via the source antenna to the receiving antenna results in heating of the sample at the terminus of the wire. By monitoring with an IR camera, three steady-state peak temperature levels were achieved: ~100 °C, ~150 °C, ~200 °C. These temperatures were chosen as they are well below any observable polymer decomposition temperature as measured by thermogravimetric analysis (Fig. S5) and the oxidation reaction temperature of Al/CuO nanothermites [17]. After achieving a steady-state temperature for ~10 s, the samples were ignited from the right-end by a secondary heat source and the combustion wave was recorded by high speed color imaging. During combustion, the MW power was left on to maintain the

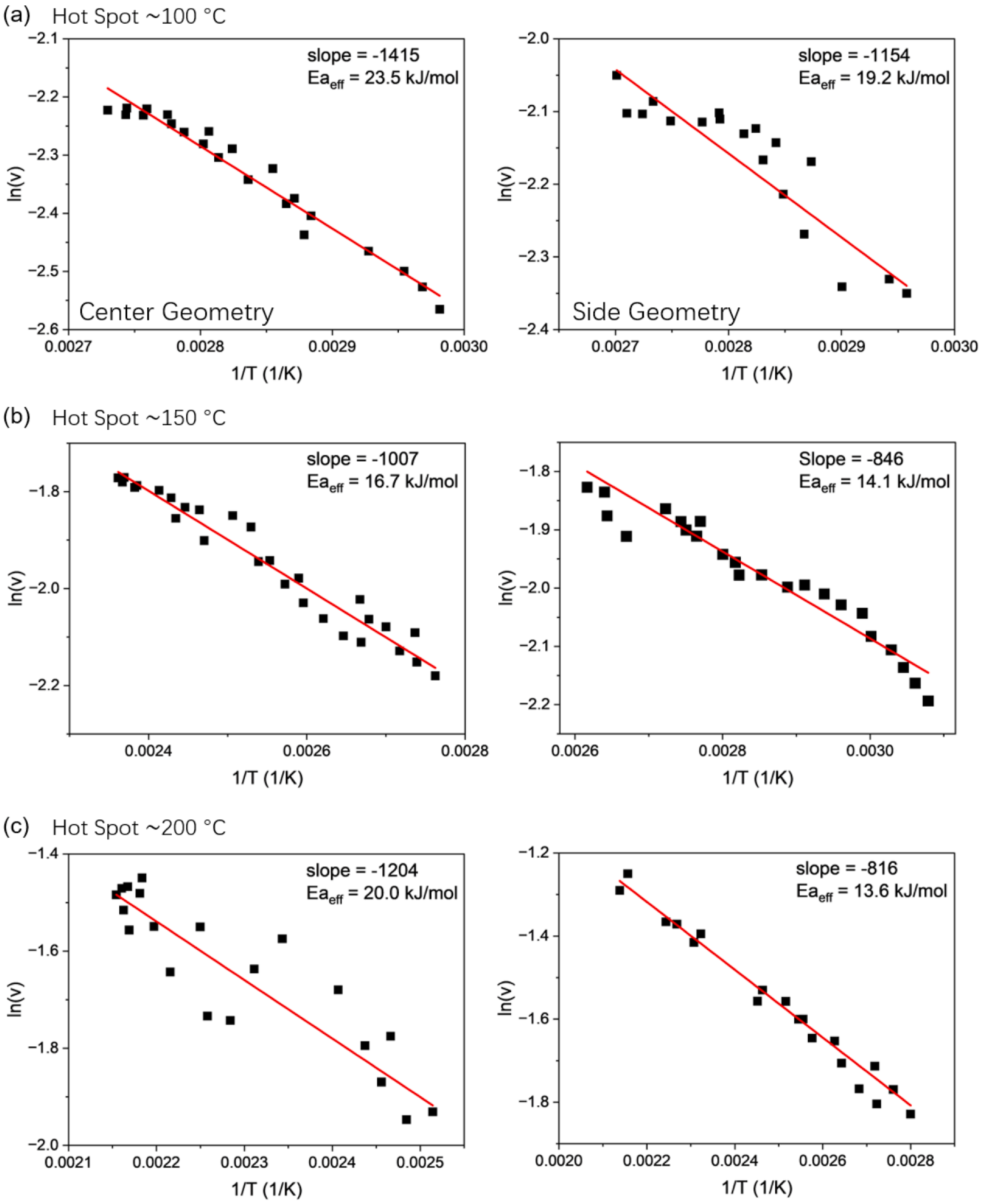

Fig. 6. Effective activation energy for the two geometries at three different initial hot spots levels. (Center geometry in left column and side geometry in right column) The average effectivity activation energy is 18 ± 4 kJ/mol.

hot spot temperature. Experiments were also conducted on the Al/CuO samples with an embedded receiving antenna for both geometries, but without MW heating (surface temperature equals room temperature) to obtain the baseline results. The results show that for either geometry, with receiving antenna embedded (**without** MW power), the flame propagates linearly at ~40 mm/s along the whole sample (Fig. S6, Video S1). This indicates that embedding metal wire did not impact the burn rate in the absence of MW.

Fig. 4 shows the induced steady state temperature profile and the instantaneous burn rate for both geometries considered. In this case the MW power used was sufficient to achieve ~100 °C peak temperature. Clearly seen is that the local burn rate tracks the general features of the MW induced temperature distribution within the sample. The local burn rate first increases and achieves a maximum local burn rate of ~120 mm/s, which also corresponds to the position of the peak in the MW heated hot spot temperature. On the falling side of the hot spot the burn rate also decreases. By increasing MW power one can achieve a higher steady-state temperature. Thus, for hot spots peaked at ~150 °C (Fig. 5) and ~200 °C (Fig. S7), the peak local burn rate increased to ~180 mm/s and ~230 mm/s respectively. These instantaneous burn rate increases were also observed with an embedded Al receiving antenna at each hot spot level (Figs. S8 to S10). Comparing the two geometries and two antenna materials, all peak local burn rates were enhanced to the same level which indicates that the burn rate increase is independent of geometrical arrangement of the embedded receiving antenna, or antenna material, but only a reflection of the initial hot spot temperature. These results show that by inducing local hot spots through MW radiation, the burn rate can be dynamically increased. These results suggest

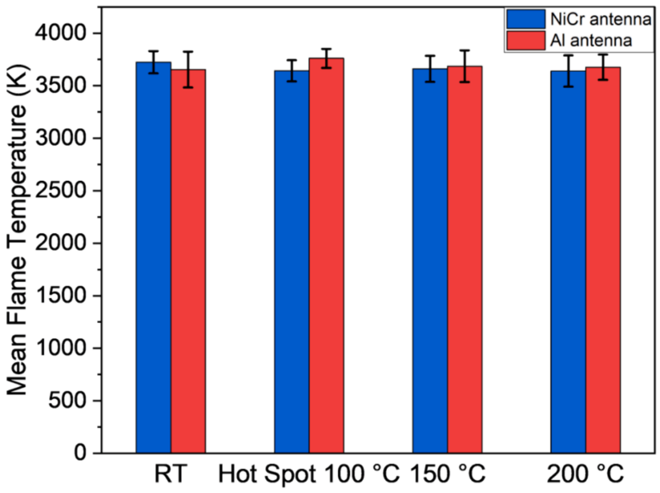

Fig. 7. Mean measured flame temperature at location of hot spots with varying initial hot spot temperature.

considerable opportunity to embed antenna at desired locations to manipulate the burn rate by a significant degree: 6×.

3.2. *Effective activation energy*

Since the local burn rates show a sensitivity to the instantaneous local temperature, an activation energy can be calculated over the hot spots profiles to assess if the local burn rate shows Arrhenius behavior. Assuming the burn rate (v) of a solid propellant is proportional to the square root of thermal diffusivity (α) and reaction rate (ω) [26,27]:

$$v \propto \sqrt{\alpha^{*}\omega} \tag{2}$$

And further assuming the reaction rate (ω) follows an Arrhenius behavior, and can be written as:

$$v \propto \sqrt{\alpha^{*}A^{*}e^{-\frac{E_{a\,eff}}{2RT}}} \tag{3}$$

If we assume α and A are temperature-independent, the burn rate can be plotted as a function of temperature in an Arrhenius plot. Fig. 6 shows Arrhenius plots for the two geometries and the three initial temperature profiles with an embedded NiCr receiving antenna. Quite clearly the behavior is Arrhenius over the whole temperature profile in the sample, and thus an effective activation energy can be calculated, to yield a value of ~18 kJ/mol (the effective activation energy calculated for embedded Al antenna is ~20 kJ/mol, Fig. S11). This is an order of magnitude lower than the reported activation energy for the chemical reaction between Al and CuO of 270 kJ/mol [28]. Such large activation energy differences have been reported for other metal/metal oxidizer systems, where a temperature profile analysis gives an activation energy an order of magnitude lower than calculated chemistry activation energy from thermal analysis [29,30]. The reader should keep in mind that the calculated effective activation energy in this study represents the temperature sensitivity to the burn rate of the high loading nanothermites samples, and thus reflects not only the intrinsic chemistry, but also the effective transport limits associated with particle–particle contacts and retardation effects of the polymer matrix [31]. To investigate which limiting effect dominates the chemical reaction, 95 wt% loading nanothermites with an embedded NiCr receiving antenna of side geometry were fabricated and tested with hot spots at ~100 °C, ~150 °C and ~200 °C (Ink composition is listed in Table S2). The 95 wt% loading samples with embedded receiving antenna propagates linearly at ~100 mm/s without MW heating. With generated hot spots at ~100 °C, ~150 °C and ~200 °C, the peak burn rate increases ~2×, ~3 × and 4.5× respectively, and the burn rate changes track the hot spots temperature profile (Fig. S12). The effective activation energy calculated from the Arrhenius plot is ~16 kJ/mol. Since the two different loading samples have similar porosity of ~60 % (Fig. S13). This suggests that at high loading condition, the chemical reaction between nanothermites is greatly limited by the diffusion process and the polymer only forms a binder matrix [32,33].

Three color pyrometry was used to measure the flame temperature when the samples propagated through the hot spots at different initial temperatures to understand the relationship between the flame temperature and local burn rate changes. Fig. 7 shows the average flame temperature for different initial temperature profiles. The results indicate that flame temperature is not sensitive to initial temperature, or MW radiation level, or at least within the uncertainty in our temperature measurement. This indicates that the main mechanism of burn rate increase is related to the localized hot spot temperature profile. The reaction rate increases with initial temperature profile of the hot spots and increases the burn rate of the nanothermites. Since the energy release rate of a solid propellant is proportional to flame temperature and burn rate. This means both burn rate and energy release rate can also be modulated, via local hot spot generated by embedding receiving antenna, and provides a new method to throttle solid propellant via localized MW energy.

4. Conclusions

In this work, localized hot spots generated by remote MW stimulation have been shown to dynamically modulate the burn rate of Al/CuO nanothermites with an embedded receiving antenna. Two embedded antenna geometries (center and side geometries), two antenna materials (NiCr and Al) and three initial MW induced hot spots temperatures (~100 °C, ~150 °C and ~200 °C) were tested. High speed color imaging shows that the local burn rate changes correspond to the initial hot spots' temperature profile. The local burn rate increase closely tracks the hot spot spatial distribution, and for our experimental condition enabled an amplification of burn rate of ~6×. It was found that the local instantaneous burn rate showed Arrhenius behavior with respect to local initial temperature enabling determination of an effective activation energy of ~18 kJ/mol. This effective activation energy represents the burn rate sensitivity to initial temperature of the high loading Al/CuO samples and likely represents the limitation of transport between the nano particles in the polymer matrix. The local burn rate increasing remain the same at different geometries and the unchanged mean flame temperature when propagated through the hot spots indicated that the main mechanism of the local burn rate increases is caused by the localized hot spot on the Al/CuO nanothermites. This experiment provides a new approach to evaluate the temperature sensitivity of solid propellant and shows that one can dynamically modulate the burn rate of solid propellants by localized MW energy.

CRediT authorship contribution statement

Keren Shi: Writing – original draft, Formal analysis, Data curation. **Yujie Wang:** Writing – review & editing, Formal analysis, Data curation. **Michael R. Zachariah:** Writing – review & editing, Supervision, Resources, Project administration, Methodology, Investigation, Funding acquisition, Conceptualization.

Declaration of competing interest

The authors declare that they have no known competing financial interests or personal relationships that could have appeared to influence the work reported in this paper.

Data availability

Data will be made available on request.

Acknowledgments

This work was supported by AFOSR and ARO.

Appendix A. Supplementary data

Supplementary data to this article can be found online at https://doi.org/10.1016/j.cej.2024.152192.

References

[1] C. Rossi, S. Orieux, B. Larangot, T. Do Conto, D. Estève, Design, fabrication and modeling of solid propellant microrocket-application to micropropulsion, Sens. Actuators, A 99 (2002) 125–133, https://doi.org/10.1016/S0924-4247(01)00900-1.

[2] K. Lysien, A. Stolarczyk, T. Jarosz, Solid propellant formulations: A review of recent progress and utilized components, Materials 14 (2021) 6657, https://doi.org/10.3390/ma14216657.

[3] A.I. Atwood, T.L. Boggs, P.O. Curran, T.P. Parr, D.M. Hanson-Parr, C.F. Price, J. Wiknich, Burning rate of solid propellant ingredients, Part 1: Pressure and initial temperature effects, J. Propul. Power 15 (1999) 740–747, https://doi.org/10.2514/2.5522.

[4] W.N. Sawka, M. McPherson, Electrical solid propellants: A safe, micro to macro propulsion technology, in: 49th AIAA/ASME/SAE/ASEE Joint Propulsion Conference, American Institute of Aeronautics and Astronautics, San Jose, CA, 2013. https://doi.org/10.2514/6.2013-4168.

[5] J.D. Hunley, The history of solid-propellant rocketry: What We Do and 'Do Not Know (Invited Paper), (n.d.).

[6] B. Gobin, N. Harvey, G. Young, Combustion characteristics of electrically controlled solid propellants using polymer electrolytes, Combust. Flame 244 (2022) 112291, https://doi.org/10.1016/j.combustflame.2022.112291.

[7] B. Duan, H. Zhang, L. Wu, Z. Hua, Z. Bao, N. Guo, Y. Ye, R. Shen, Controllable combustion behaviors of the laser-controlled solid propellant, Defence Technol. 18 (2022) 38–48, https://doi.org/10.1016/j.dt.2021.03.002.

[8] J. Napior, V. Garmy, Controllable solid propulsion for launch vehicle and spacecraft application, in: 57th International Astronautical Congress, American Institute of Aeronautics and Astronautics, Valencia, Spain, 2006. https://doi.org/10.2514/6.IAC-06-C4.2.04.

[9] K.K. Kuo, R. Acharya, Applications of Turbulent and Multiphase Combustion, 1st ed., Wiley, 2012. https://doi.org/10.1002/9781118127575.

[10] D. Lim, K. Gnanaprakash, R. Rajak, J.J. Yoh, Combustion behavior of electrically controlled solid propellant with tungsten additive, Thermochim. Acta 727 (2023) 179562, https://doi.org/10.1016/j.tca.2023.179562.

[11] H. Wang, E. Hagen, K. Shi, S. Herrera, F. Xu, M.R. Zachariah, Carbon fibers as additives to engineer agglomeration and propagation of aluminized propellants, Chem. Eng. J. (2023) 141653, https://doi.org/10.1016/j.cej.2023.141653.

[12] S. Isert, C.D. Lane, I.E. Gunduz, S.F. Son, Tailoring burning rates using reactive wires in composite solid rocket propellants, Proc. Combust. Inst. 36 (2017) 2283–2290, https://doi.org/10.1016/j.proci.2016.06.141.

[13] P.N. Dave, R. Sirach, R. Thakkar, Thermal decomposition and kinetic investigation of AP and AP based composite solid propellant in the presence of nickel ferrite additive, J. Mater. Res. Technol. 19 (2022) 4183–4196, https://doi.org/10.1016/j.jmrt.2022.06.123.

[14] S. Isakari, T. Asakura, D. Haraguchi, Y. Yano, A. Kakami, Performance evaluation and thermography of solid-propellant microthrusters with laser-based throttling, Aerosp. Sci. Technol. 71 (2017) 99–108, https://doi.org/10.1016/j.ast.2017.08.027.

[15] S.J. Barkley, K. Zhu, J.E. Lynch, J.B. Michael, T.R. Sippel, Microwave plasma enhancement of multiphase flames: On-demand control of solid propellant burning rate, Combust. Flame 199 (2019) 14–23, https://doi.org/10.1016/j.combustflame.2018.10.007.

[16] W.H. Sutton, Microwave processing of materials, MRS Bull. 18 (1993) 22–29, https://doi.org/10.1017/S0883769400038495.

[17] H. Wang, D.J. Kline, M.C. Rehwoldt, M.R. Zachariah, Carbon fibers enhance the propagation of high loading nanothermites. in situ observation of microscopic combustion, ACS Appl. Mater. Interfaces 13 (2021) 30504–30511, https://doi.org/10.1021/acsami.1c02911.

[18] K. Shi, Y. Wang, F. Xu, M.R. Zachariah, Remote microwave heating and ignition with an embedded receiving antenna within nanocomposites, Chem. Eng. Sci. 280 (2023) 118948, https://doi.org/10.1016/j.ces.2023.118948.

[19] D. Bradley, G. Roth, Adaptive thresholding using the integral image, J. Graph. Tools 12 (2007) 13–21, https://doi.org/10.1080/2151237X.2007.10129236.

[20] R.J. Jacob, D.J. Kline, M.R. Zachariah, High speed 2-dimensional temperature measurements of nanothermite composites: Probing thermal vs. Gas generation effects, J. Appl. Phys. 123 (2018) 115902, https://doi.org/10.1063/1.5021890.

[21] Y. Wang, E. Hagen, P. Biswas, H. Wang, M.R. Zachariah, Imaging the combustion characteristics of Al, B, and Ti composites, Combust. Flame 252 (2023) 112747, https://doi.org/10.1016/j.combustflame.2023.112747.

[22] Standard Specification for Drawn or Rolled Nickel-Chromium and Nickel-Chromium-Iron Alloys for Electrical Heating Elements, ASTM International.

[23] P. Biswas, G.W. Mulholland, M.C. Rehwoldt, D.J. Kline, M.R. Zachariah, Microwave absorption by small dielectric and semi-conductor coated metal particles, J. Quant. Spectrosc. Radiat. Transf. 247 (2020) 106938, https://doi.org/10.1016/j.jqsrt.2020.106938.

[24] Y.A. Lebedev, Microwave discharges: generation and diagnostics, J. Phys. Conf. Ser. 257 (2010) 012016, https://doi.org/10.1088/1742-6596/257/1/012016.

[25] C. Gabriel, S. Gabriel, E.H. Grant, E.H. Grant, B.S.J. Halstead, D. Michael, P. Mingos, Dielectric parameters relevant to microwave dielectric heating, Chem. Soc. Rev. 27 (1998) 213, https://doi.org/10.1039/a827213z.

[26] L.C. Mallard, Recherches sur la combustion des mélanges gazeux explosifs, J. Phys. Theor. Appl. 4 (1885) 59–84, https://doi.org/10.1051/jphystap:01885004005901.

[27] C.K. Law, Combustion Physics, 1st ed., Cambridge University Press, 2006. https://doi.org/10.1017/CBO9780511754517.

[28] S.M. Umbrajkar, M. Schoenitz, E.L. Dreizin, Exothermic reactions in Al–CuO nanocomposites, Thermochim Acta 451 (2006) 34–43, https://doi.org/10.1016/j.tca.2006.09.002.

[29] A.S. Mukasyan, C.E. Shuck, Kinetics of SHS reactions: A review, Int. J. Self Propag. High Temp. Synth. 26 (2017) 145–165, https://doi.org/10.3103/S1061386217030049.

[30] D.J. Kline, M.C. Rehwoldt, J.B. DeLisio, S.C. Barron, H. Wang, Z. Alibay, J. C. Rodriguez, G.M. Fritz, M.R. Zachariah, In-operando thermophysical properties and kinetics measurements of Al-Zr-C composites, Combust. Flame 228 (2021) 250–258, https://doi.org/10.1016/j.combustflame.2020.12.045.

[31] R.L. Drennan, M.E. Brown, Binary and ternary pyrotechnic systems of Mn and/or MO and Ba02 and/or Sr02. Part 3. Kinetic aspects, (n.d.).

[32] T. Boddington, P.G. Laye, J. Tipping, D. Whalley, Kinetic analysis of temperature profiles of pyrotechnic systems, Combust. Flame 63 (1986) 359–368, https://doi.org/10.1016/0010-2180(86)90005-2.

[33] C.R. Kachelmyer, A. Varma, A.S. Rogachev, A.E. Sytschev, Influence of reaction mixture porosity on the effective kinetics of gasless combustion synthesis, Ind. Eng. Chem. Res. 37 (1998) 2246–2249, https://doi.org/10.1021/ie9704915.